

Supporting Information for

Molecular Engineering Accelerated Polarity Switching Enabling High-Performance n-Type Organic Thermoelectrics

Fei Zhong,^a Xiaojun Yin,^{a,*} Jiatao Wu,^b Chunmei Gao,^b Cheng Zhong,^c and Lei Wang^{a,*}

^aShenzhen Key Laboratory of Polymer Science and Technology, College of Materials Science and Engineering, Shenzhen University, Shenzhen 518060, China.

^bCollege of Chemistry and Chemical Engineering, Shenzhen University, Shenzhen 518060, PR China.

^cHubei Key Lab on Organic and Polymeric Optoelectronic Materials, Department of Chemistry, Wuhan University, Wuhan, 430072, P. R. China.

*E-mail: xiaojunyin@szu.edu.cn, wl@szu.edu.cn

Table of contents

General Information.....	2
Materials and Syntheses	4
Concepts of the Seebeck coefficient.....	6
Photophysical, electrochemical and thermal properties.	7
OFET measurements.	10
Progress of the n-type polymer thermoelectrics.	12
Table S3. Representative progress of the n-type organic polymer thermoelectrics.	13
Temperature-dependence conductivity and Seebeck Coefficient measurements.....	14
X-Ray Diffraction measurements.	15
Theoretical calculations	16
References.....	22

General Information

^1H NMR spectra were recorded on a Bruker AVANCE III 500 MHz NMR spectrometer in CDCl_3 using tetramethylsilane as internal standard. The molecular weight (M_n , M_w) and distribution (PDI) of the polymers were measured by Waters e2695 Separations Module (Waters, Singapore) using tetrahydrofuran as eluent. The UV-Vis-NIR absorption spectra of these polymer thin films were collected from Lambda 950 (PerkinElmer, Waltham, MA, USA) spectrophotometer. Cyclic voltammetry (CV) measurements were taken on a CHI 660 workstation. The drop-casting polymer films were measured in acetonitrile solution under the nitrogen atmosphere with tetrabutylammonium hexafluorophosphate (0.1 M) as the electrolyte. The platinum disk electrode was used as the working electrode and the platinum wire was used as the counter electrode, and the Ag/AgCl electrode was used as the reference electrode, commonly used ferrocenium-ferrocene (Fc^+/Fc) acting as the internal standard, with the scanning rate of 50 mV s^{-1} . The onset potential (E_{onset}) was determined from the intersection of two tangents drawn at the rising and background current of the cyclic voltammogram, and the HOMO or LUMO energy levels (eV) of these compounds are calculated according to the formula: $-[4.8 \text{ eV} + (E_{\text{onset}} - E_{1/2(\text{Fc}/\text{Fc}^+)})]$. Thermogravimetric analysis (TGA) was tested on a TGA-55 system (TA Instruments, New Castle, DE, USA) with a heating rate of $10 \text{ }^\circ\text{C}/\text{min}$ under nitrogen. Grazing Incidence X-ray Diffraction (GIXRD) were collected on an X-ray diffractometer (SmartLab, Japan) with a Cu target ($\lambda = 1.54 \text{ \AA}$). Diffraction patterns were obtained at a scan rate of 5° min^{-1} . Ultraviolet photoemission spectroscopy (UPS) data was collected using an ESCALAB 250Xi X-ray photoelectron spectrometer with a He I (21.22 eV) gas discharge lamp source and a monochromatic Al $K\alpha$ source as the excitation source.

Methods

Thin film samples preparation. Firstly, the polymer samples were completely dissolved in appropriate anhydrous *o*-dichlorobenzene/chlorobenzene (1:1, v/v) to give 7.5 mg mL^{-1} fresh standby solution, respectively. The precleaning glass substrates ($1 \times 1 \text{ cm}$) were sonicated with deionized water, acetone, and isopropanol successively, and drying with argon flow. Then, the fresh polymer solutions were evenly dropped onto the glass substrates with unified volume of $80 \text{ }\mu\text{L}$, and the solvent was evaporated slowly at the ambient condition to produce the free-standing

thin films with similar thickness of around 3 μm . The formed thin films were directly doped with different p-dopants (FeCl_3 , AuCl_3 , or magic blue) at different concentrations (0.01 M, 0.025 M, 0.05 M, 0.1 M, 0.2 M, or 0.5 M) in acetonitrile solutions with uniform duration time of 5 min (at ambient condition). The residual dopants were washed with pure acetonitrile, and then drying with argon flow.

Thermoelectric measurements. The key data including S and σ both at room temperature (300 K) and variable temperature conditions (200-350 K) were collected in an integrative thermoelectric parameters test system (MRS, Joule Yacht, China) ¹. To verify the accuracy of measurements, the S of the standard Ni was tested as the internal reference standard, and the results ($-16.2 \pm 0.3 \mu\text{V K}^{-1}$) was confirmed with the normal data. For each data point, an average of four polymer samples was measured for cross-checking. The thickness of these doped thin films was determined by step profiler (ET-4000M, Kosaka Laboratory Ltd., Tokyo, Japan).

EPR measurements. The EPR spectra of these polymer samples were recorded on Bruker EMXPlus-10/12, with consistent microwave frequency (9.8 GHz), and power (2.0 mW). The temperature-dependence EPR spectra were obtained from Bruker EMXPlus-10/12 at 100K, 200K, and 300K, respectively. To exclude the influence of metal ion on magnetic field, p-dopant of FeCl_3 or AuCl_3 were equivalently replaced with NOBF_4 . Polymer thin films employed in EPR measurements were prepared in line with the thermoelectric samples, and the different concentrations of dopant solutions were prepared by slowly dissolve different loading of NOBF_4 in anhydrous acetone under ice-bath. The doped polymer thin films were carefully scraped off the glass substrates and rapidly transferring to the EPR tube, and then charged with argon. All these fresh EPR samples with equal quantity ($\sim 0.6 \text{ mg}$) were instantaneously measured within 3 hours.

DFT calculations. All of the theoretical calculations were performed using the Gaussian 16 program package. The geometries of these polymer models at both ground states and corresponding radical cations were optimized at B3LYP-D3(BJ)/def2svp level. The calculations of open-shell radical cations were carried out in diphenylether solution based on the ground state geometries. The electronic properties of these open-shell radicals were calculated *via* DFT procedure using optimally tuned range-separated exchange density functions at the LC-

ω pbex/def2svp level, and the ω tuning was implemented whereby iterative, nonempirical ionization potential tuning procedure². The HOMO/LUMO distributions, surface electrostatic potential distribution and orbital overlaps were visualized using Gaussview 6.0. The TDOS curves from the ground state (neutral) to corresponding radical cation state (p-doped form), as well as the overlap integral of norm of the two orbitals and centroid distance between the two orbitals (Angstrom) were analyzed using the Multiwfn 3.8 program³.

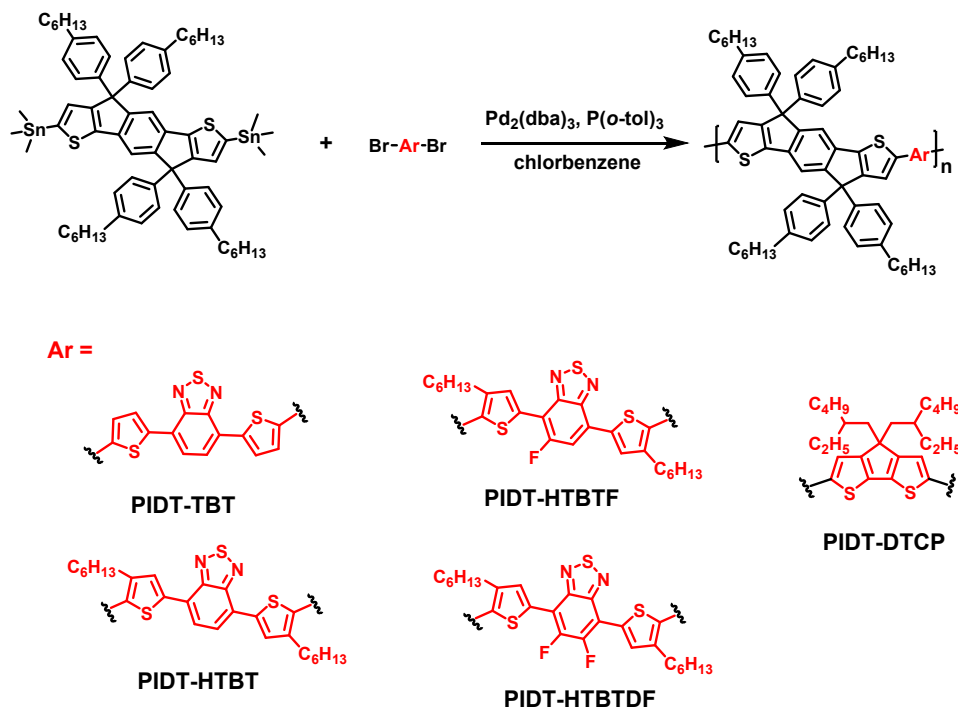
Materials and Syntheses

Commercially available reagents and solvents involved in this work were used directly without further processing unless otherwise mentioned. Key intermediates of (4,4,9,9-tetrakis(4-hexylphenyl)-4,9-dihydro-*s*-indaceno[1,2-*b*:5,6-*b'*]dithiophene-2,7-diyl)bis(trimethylstannane), 4,7-bis(5-bromo-4-hexylthiophen-2-yl)benzo[*c*][1,2,5]thiadiazole, 4,7-bis(5-bromo-4-hexylthiophen-2-yl)-5-fluorobenzo[*c*][1,2,5]thiadiazole, 4,7-bis(5-bromo-4-hexylthiophen-2-yl)-5,6-difluorobenzo[*c*][1,2,5]thiadiazole, 2,6-dibromo-4,4-bis(2-ethylhexyl)-4*H*-cyclopenta[2,1-*b*:3,4-*b'*]dithiophene and PCZ-TBT were purchased from Sun Tech. Inc. or Derthon optoelectronic materials science technology Co. LTD. The investigated p-dopants of FeCl₃, AuCl₃, tris(4-bromophenyl)ammoniumyl hexachloroantimonate (magic blue) and NOBF₄ with high purity (> 99%) were obtained from Sigma-Aldrich (USA) or Energy Chemical, and the existing p-type polymer host of PIDT-TBT was synthesized according to the literature method.⁴

General procedure for Pd-catalyzed Stille cross-coupling polymerization reaction

(4,4,9,9-tetrakis(4-hexylphenyl)-4,9-dihydro-*s*-indaceno[1,2-*b*:5,6-*b'*]dithiophene-2,7-diyl)bis(trimethylstannane) (1.5 mmol, 1.0 equivalent) and corresponding aromatic dibromide monomers (1.5 mmol, 1.0 equivalent) were dissolved in 10 mL anhydrous chlorobenzene in a 25 mL Schlenk tube. Afterwards, Pd₂(dba)₃ (0.05 equivalent) and P(*o*-tol)₃ (0.25 equivalent) were added subsequently into the aforementioned mixture. The mixture was deoxidized by a freeze-pump-thaw method. Then, the mixture was allowed to stir at 110 °C for 48 h. After cooling down, the concentrated solution was precipitated with excess methanol. Further purification was executed by using Soxhlet extractor with the extraction solvent of methanol, acetone and hexane successively to remove the low molecular weight oligomers or monomers. Finally, the desirable

compounds were extracted with chloroform and removing the solvent to give the corresponding target polymers.



Scheme S1. Synthetic route of these IDT-based polymers.

PIDT-HTBT (yield 76%): ^1H NMR (500 MHz, CDCl_3) δ [ppm]: 7.98 (br, 2H), 7.83 (br, 2H), 7.48 (br, 2H), 7.26-7.25 (m, 8 H), 7.20 (br, 2H), 7.13-7.12 (m, 8 H), 2.89 (br, 4H), 2.62-2.59 (m, 8H), 1.77 (br, 4H), 1.65-1.61 (m, 8 H), 1.47 (br, 4H), 1.37-1.28 (m, 32H), 0.94-0.89 (m, 18H). $M_n = 35.6$ kDa, $M_w = 73.1$ kDa, PDI = 2.05.

PIDT-HTBTF (yield 79%): ^1H NMR (500 MHz, CDCl_3) δ [ppm]: 8.11 (br, 1H), 7.98 (br, 1H), 7.75-7.73 (m, 2H), 7.48 (br, 2H), 7.26-7.25 (m, 8 H), 7.22 (br, 2H), 7.13-7.12 (m, 8 H), 2.90 (br, 4H), 2.62-2.59 (m, 8H), 1.77 (br, 4H), 1.64-1.62 (m, 8 H), 1.47 (br, 4H), 1.37-1.28 (m, 32H), 0.93-0.89 (m, 18H). $M_n = 40.6$ kDa, $M_w = 103.3$ kDa, PDI = 2.55.

PIDT-HTBTDF (yield 84%): ^1H NMR (500 MHz, CDCl_3) δ [ppm]: 8.12 (br, 2H), 7.49 (br, 2H), 7.26-7.24 (m, 10H), 7.13-7.12 (m, 8 H), 2.90 (br, 4H), 2.62-2.59 (m, 8H), 1.76 (br, 4H), 1.65-

1.60 (m, 8 H), 1.47 (br, 4H), 1.37-1.28 (m, 32H), 0.94-0.89 (m, 18H). $M_n = 43.0$ kDa, $M_w = 99.4$ kDa, PDI = 2.31.

PIDT-DTCP (yield 72%): ^1H NMR (500 MHz, CDCl_3) δ [ppm]: 7.34-7.20 (m, 14H), 7.11 (br, 8H), 2.59 (br, 8H), 1.89-1.78 (m, 4H), 1.62-1.57 (m, 12 H), 1.36-1.28 (m, 24H), 1.03-0.89 (m, 26H), 0.73-0.64 (m, 12H). $M_n = 61.2$ kDa, $M_w = 117.8$ kDa, PDI = 1.93.

Concepts of the Seebeck coefficient.

According to the definition,⁵ the Seebeck effect, which originates from the entropically driven diffusion of charge carriers, and the Seebeck coefficient (S) can be deduced as the following expression (equation S1):

$$S = -\frac{k_B}{q} \int_{-\infty}^{+\infty} \frac{E - E_F}{k_B T} \cdot \frac{\sigma(E)}{\sigma} dE \quad (S1)$$

wherein, k_B is the Boltzmann constant, q is the elementary charge, T is temperature, E_F is the Fermi levels, and $\sigma(E)$ is the energy-dependence conductivity. Obviously, various energy levels involved in is of vital important. To well elucidate the essential factors of S , firstly, the concepts of transport levels (E_{Tr}) is proposed. Notably, the E_{Tr} is defined as the averaged energy of the charge carriers which contributed to the conduction of the samples, weighted by the conductivity distribution.²

$$E_{Tr} = \frac{1}{\sigma} \int_{-\infty}^{+\infty} E \cdot \sigma(E) dE \quad (S2)$$

Therefore, the equation S1 can be simplified as following:

$$S = \frac{E_F - E_{Tr}}{qT} = \frac{E_S}{qT} \quad (S3)$$

wherein, E_S is termed as the Seebeck energy, $E_S = E_F - E_{Tr}$. Noticeably, the S is largely relying on the relative position of E_F and E_{Tr} , and endeavors to elevate their E_{Tr} as well as to reduce their E_F is beneficial to realize n-type charge transport via p-doping. Separately, E_F is depended on the doping levels, and E_{Tr} is depended on the energy distributions of charge carriers.

Photophysical, electrochemical and thermal properties.

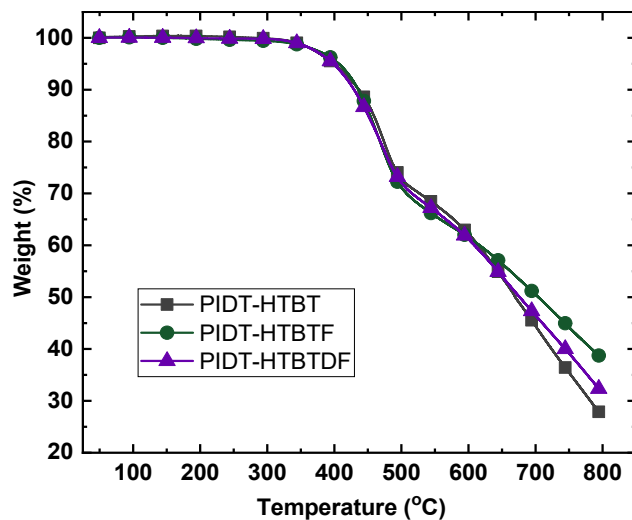


Figure S1. TGA curves of PIDT-HTBT, PIDT-HTBTF, and PIDT-HTBTDF.

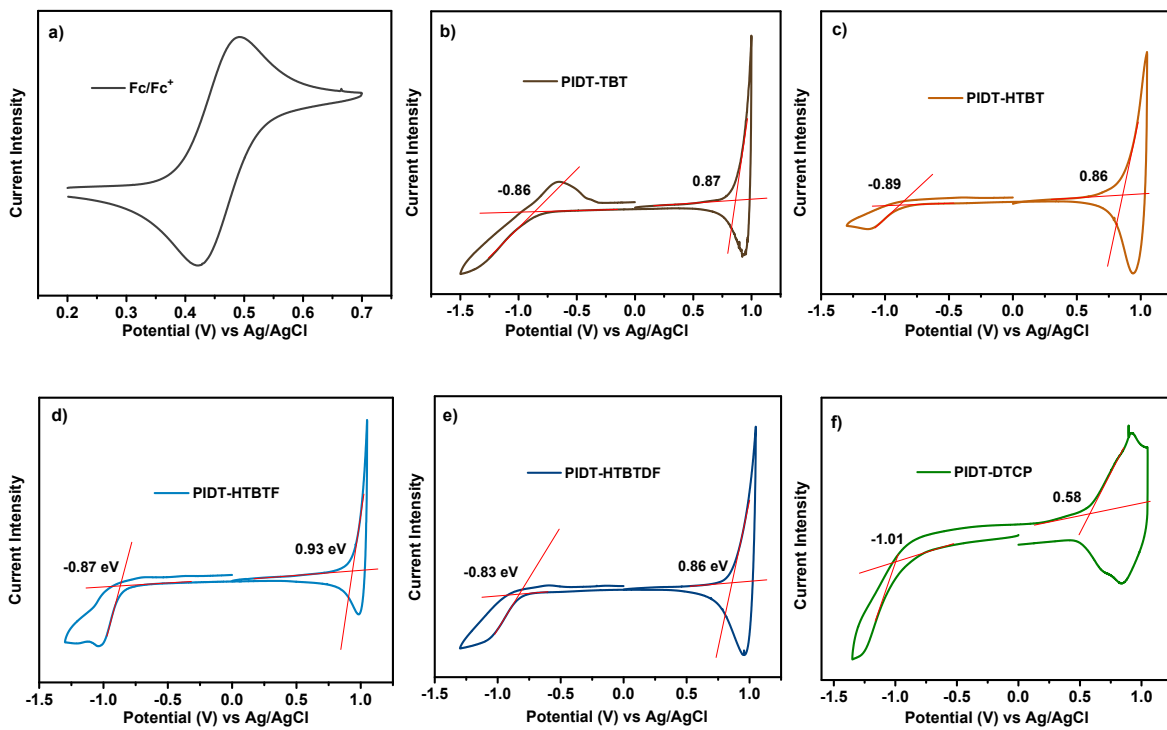


Figure S2. Cyclic voltammetry curves of these polymers.

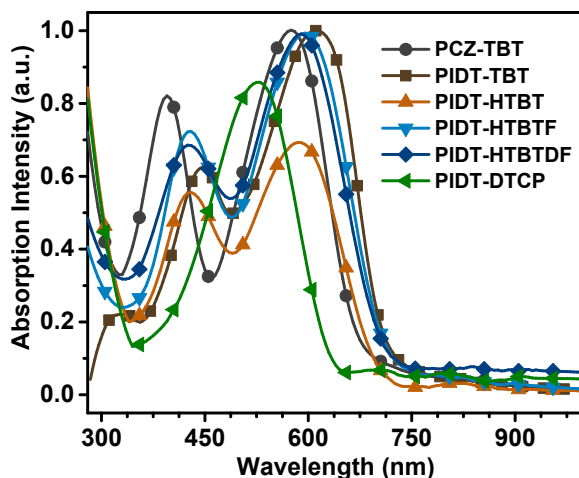


Figure S3. UV-Vis-NIR absorption spectra of these investigated polymers in films.

Notably, all the donor-acceptor (D-A) type polymers show two distinct absorption bands assigning to the typical intramolecular charge transfer transition (long wavelength region) and π - π^* transition (short wavelength region), while the PIDT-DTCP shows only one absorption peak at visible region (527 nm), indicating a typical donor-donor (D-D) type polymer.

Table S1. Photophysical, electrochemical and thermal data of these polymers.

Polymers	LUMO/HOMO [eV] ^{a)}	E_g^{ele} [eV] ^{b)}	E_g^{opt} [eV] ^{c)}	$\lambda_{\text{abs,max}}$ [nm] ^{d)}	T_d [°C] ^{e)}
PCZ-TBT	-3.30/-5.15 ^{f)}	1.85	1.86	395, 575	470 ^{f)}
PIDT-TBT	-3.48/-5.21	1.73	1.74	447, 611	392 ^{f)}
PIDT-HTBT	-3.45/-5.20	1.75	1.77	428, 586	399
PIDT-HTBTF	-3.47/-5.27	1.80	1.74	428, 593	407
PIDT-HTBTDF	-3.51/-5.20	1.69	1.76	428, 589	399
PIDT-DTCP	-3.33/-4.92	1.59	1.97	527	388 ^{f)}

^{a)}Estimated from the cyclic voltammetry curves of these polymer films, ^{b)}calculated from the difference values between the HOMOs and corresponding LUMOs ($E_g^{\text{ele}} = E_{\text{LUMO}} - E_{\text{HOMO}}$), ^{c)}obtained from the optical absorption edge in films, ^{d)}measured from their UV-Vis-NIR absorption spectra, ^{e)}determined from their TGA curves, ^{f)}obtained from the previously reported works.^{4,6}

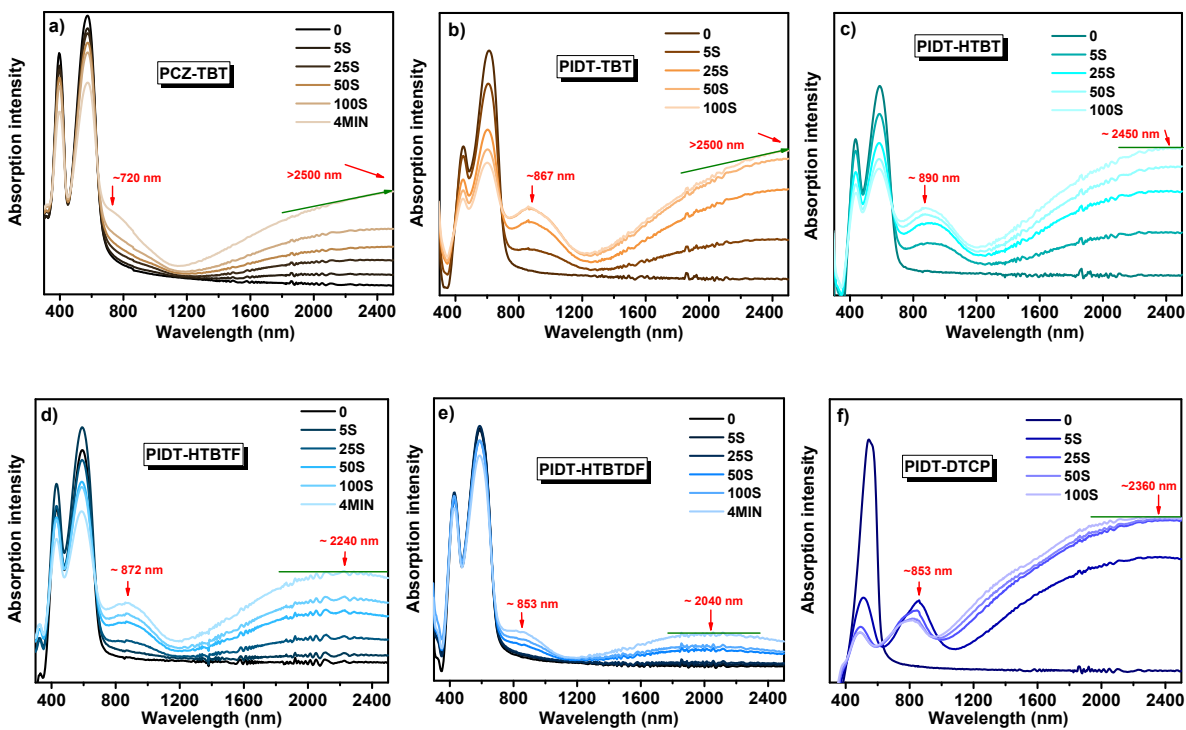


Figure S4. The UV-Vis-NIR absorption spectra of the involved six polymers in films, doped with $0.025 \text{ mmol L}^{-1} \text{ FeCl}_3$ acetonitrile solution at different doping times. a)-f) for PCZ-TBT, PIDT-TBT, PIDT-HTBT, PIDT-HTBTF, PIDT-HTBTDF, and PIDT-DTCN, respectively.

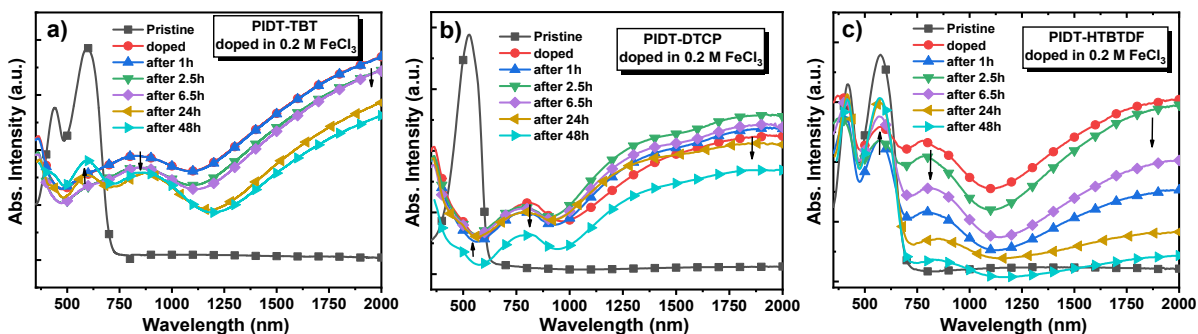


Figure S5. The air-stability of these doped polymer films, a) PIDT-TBT, b) PIDT-DTCP, c) PIDT-HTBTDF.

OFET measurements.

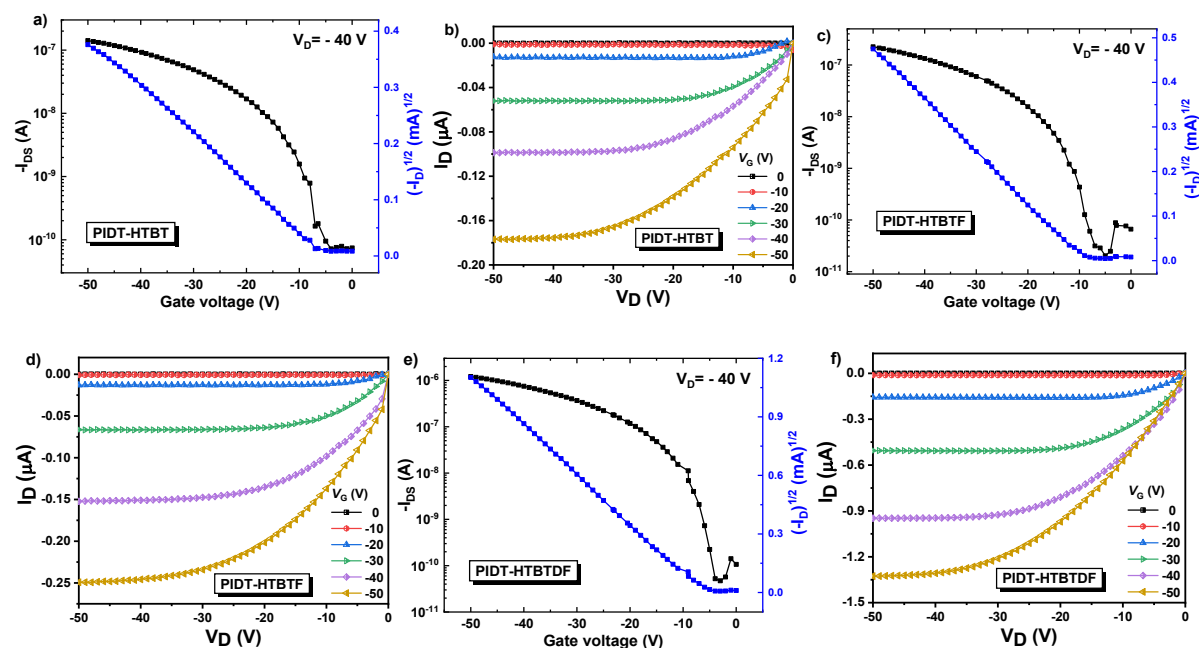


Figure S6. The output curves and transfer curves of these OFET devices. Output curves/ transfer curves for PIDT-HTBT (a/b), PIDT-HTBTF (c/d) and PIDT-HTBTDF (e/f) based OFET devices, respectively.

Table S2. Key data of these OFET devices.

Polymer	$\mu_{\text{OFET}} (\text{cm}^2 \text{V}^{-1} \text{s}^{-1})$	$V_T (\text{V})$	$I_{\text{on}}/I_{\text{off}}$
PIDT-HTBT	1.57×10^{-3}	-2.0	1.9×10^3
PIDT-HTBTF	1.32×10^{-3}	-6.8	3.4×10^3
PIDT-HTBTDF	1.24×10^{-2}	-2.3	1.2×10^4

OFET measurements were performed to discuss the introduction of F atoms and structural regularity on influencing their intrinsic charge transport properties. Notably, PIDT-HTBTDF with difluoro-diazosulfide acceptors demonstrated the best OFET performances, which can be attribute to the higher structural regularity and F-H interaction beneficial to modulate their intermolecular-packing and charge transfer.

Table S3. Key TE data of these polymers with different p-doping.

Polymers	p-type ^{a)}			n-type ^{a)}		
	S [$\mu\text{V K}^{-1}$]	σ [S cm^{-1}]	PF [$\mu\text{W m}^{-1} \text{K}^{-2}$]	S [$\mu\text{V K}^{-1}$]	σ [S cm^{-1}]	PF [$\mu\text{W m}^{-1} \text{K}^{-2}$]
PCZ-TBT	34.5 ± 1.3	98.0 ± 3.4	11.7 ± 0.5	-- ^{b)}	--	--
PIDT-TBT	34.7 ± 0.6	22.7 ± 1.5	2.72 ± 0.1	--	--	--
PIDT-HTBT	48.6 ± 2.5	4.0 ± 0.3	0.9 ± 0.1	-51.1 ± 3.3	4.6 ± 1.0	1.2 ± 0.1
PIDT-HTBTf	32.3 ± 1.6	4.9 ± 0.3	0.5 ± 0.1	-87.2 ± 2.6	3.0 ± 0.3	2.26 ± 0.3
PIDT-HTBTDF	160.0 ± 1.6	4.8 ± 0.2	12.2 ± 0.3	-177.3 ± 4.1	6.6 ± 0.4	20.7 ± 0.3
PIDT-DTCP	152.2 ± 1.5	0.1 ± 0.0	0.2 ± 0.0 ^{c)}	-85.3 ± 4.8	0.1 ± 0.0	0.1 ± 0.0

^{a)}Both p-type and n-type TE values were collected by doping with p-dopant FeCl_3 , only the p-type TE values of PIDT-HTBTDF were optimized with magic blue. ^{b)}Not obtained due the unprocurable of polarity switching. ^{c)}The data 0.0 means lower than 0.1.

Table S4. Air-stability of these heavily p-doped (0.5 M in FeCl_3) polymer samples.

PCZ-TBT	Exposure duration [min]	0	944	1530	1792	2760
	S [$\mu\text{V K}^{-1}$]	15.7	15.0	17.35	18.5	20.1
	σ [S cm^{-1}]	153.8	153.3	151.8	148.9	135.9
PIDT-DTCP	Exposure duration [min]	0	162	514	747	1643
	S [$\mu\text{V K}^{-1}$]	-99.2	-65.9	-34.3	-43.9	-10.3
	σ [S cm^{-1}]	0.11	0.11	0.11	0.13	0.16
PIDT-HTBTDF	Exposure duration [min]	0	1210	1442	2061	2692
	S [$\mu\text{V K}^{-1}$]	-184.6	-57.2	-39.7	-45.1	-15.7
	σ [S cm^{-1}]	2.15	2.24	2.39	2.68	2.82

Notably, the PCZ-TBT film remain p-type feature even in 0.5 M FeCl_3 solution, and negligible changes can be observed on both the S and σ values along with the increase of exposure times. However, obvious decay of S occurs on these n-type samples, which may due to the de-doping and electron trapping mechanism. Accordingly, the σ values of these n-type samples were only slightly enhanced resulting in gradually degenerating in power factors.

Progress of the n-type polymer thermoelectrics.

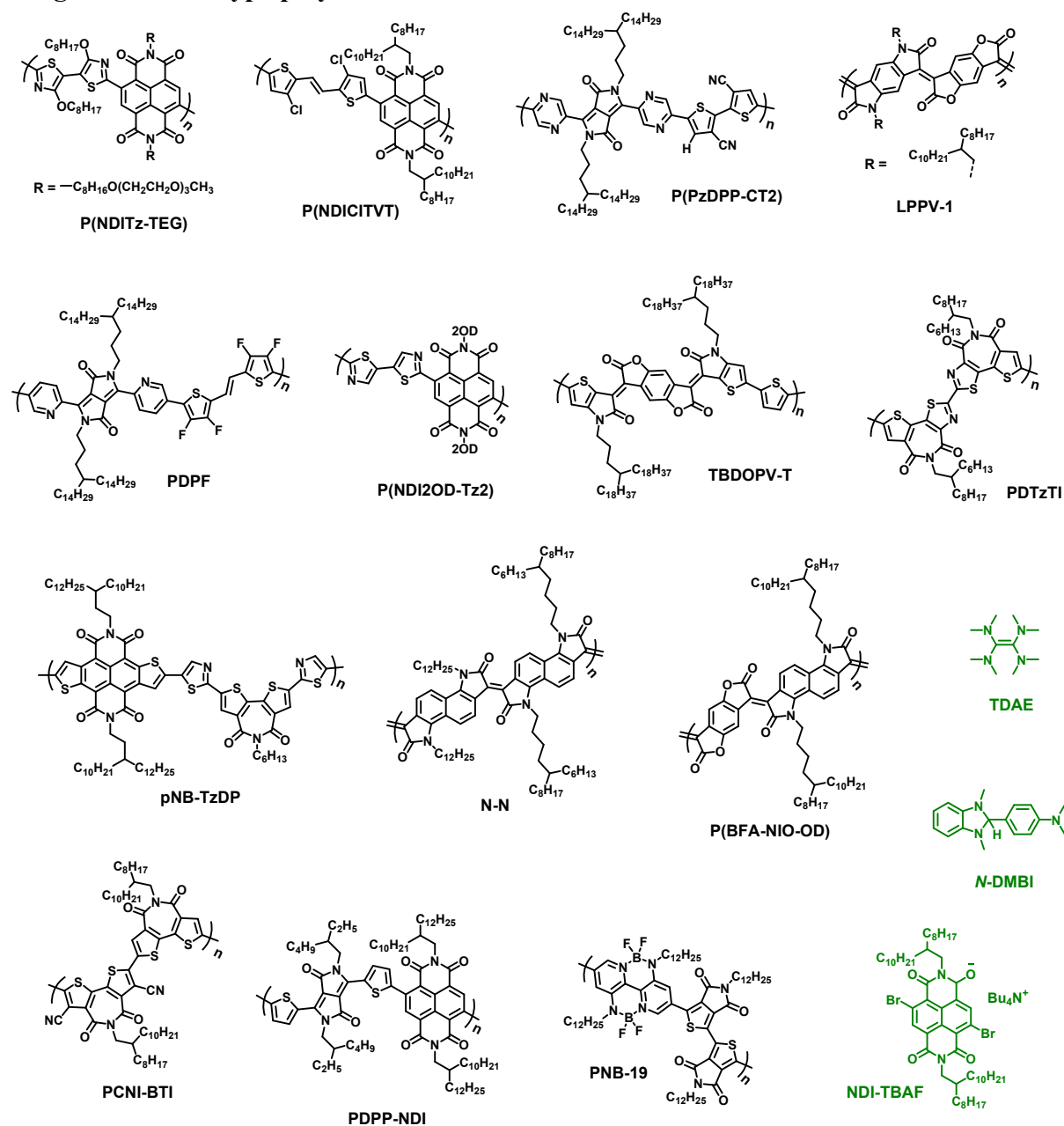


Figure S7. Chemical structures of the representative n-type organic polymer thermoelectric materials via conventional n-doping.

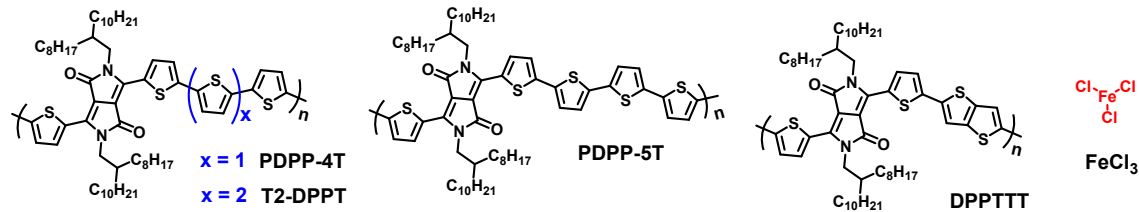


Figure S8. N-type organic thermoelectric realized from p-doping.

Table S5. Representative progress of the n-type organic polymer thermoelectrics.

Polymer Host	Dopants ^{a)}	Doping method	Process	S [$\mu\text{V K}^{-1}$]	σ [S cm^{-1}]	PF [$\mu\text{W m}^{-1} \text{K}^{-2}$]	Ref.
PDTzTI	TDAE	soaking	spin-coating	-129	4.6	7.6	7
LPPV-1	N-DMBI	blending	spin-coating	133.5	1.1	1.96	8
P(PzDPP-CT2)	N-DMBI	blending	spin-coating	-378	4.0	57.3	9
P(BFA-NIO-OD)	N-DMBI	blending	spin-coating	-75	0.28	0.16	10
PDPP-NDI	N-DMBI	blending	drop-casting	-271.1	0.38×10^{-3}	2.83×10^{-3}	11
P(NDITz-TEG)	N-DMBI	blending	spin-coating	-326 ± 31	1.6 ± 0.1	16.5 ± 1.2	12
pNB-TzDP	N-DMBI	blending	spin-coating	-214	11.6	53.4	13
N-N	N-DMBI	blending	spin-coating	-222	0.65	3.2	14
PNB-19	TDAE	Vapor	spin-coating	-178.8	7.8	24.8	15
PCNI-BTI	N-DMBI	blending	spin-coating	-83.3	23.3	10	16
PNDICITVT	NDI-TBAF	blending	spin-coating	-1854	0.2	67	17
PDFP	N-DMBI	blending	spin-coating	-235	1.30	4.65	18
P(NDI2OD-Tz2)	TDAE	Vapor	spin-coating	-447 ± 15	0.06	1.5	19
TBDOPV-T	N-DMBI	blending	spin-coating	-135 ± 6	53 ± 6	96 ± 10	20
PDPP-5T	FeCl ₃	blending	spin-coating	-28	124	~ 10	21
PDPP-4T	FeCl ₃	blending	spin-coating	-74	16.8	9.2	2
DPPTTT	FeCl ₃	blending	drop-casting	-20.25	14.22	0.66	22
T2-DPPT	FeCl ₃	blending	spin-coating	-129.5	0.10	0.17	23
PDPP-4T	FeCl ₃	blending	spin-coating	-82.2	0.32	0.22	23
PIDT-HTBTDF	FeCl₃	soaking	drop-casting	-177.3 ± 4.1	6.6 ± 0.4	20.7 ± 0.3	This work
PIDT-HTBTDF	FeCl₃	soaking	drop-casting	-208.7 ± 0.6	2.0 ± 0.6	8.6 ± 2.7	This work
PIDT-HTBTDF	AuCl₃	soaking	drop-casting	-80.8 ± 1.6	14.5 ± 0.4	9.5 ± 0.1	This work

^{a)}Notacibaly, n-dopants of TDAE, N-DMBI, NDI-TBAF relating to the n-doping, and the last five rows using p-dopants of FeCl₃ or AuCl₃ concerning p-doping.

Temperature-dependence conductivity and Seebeck Coefficient measurements

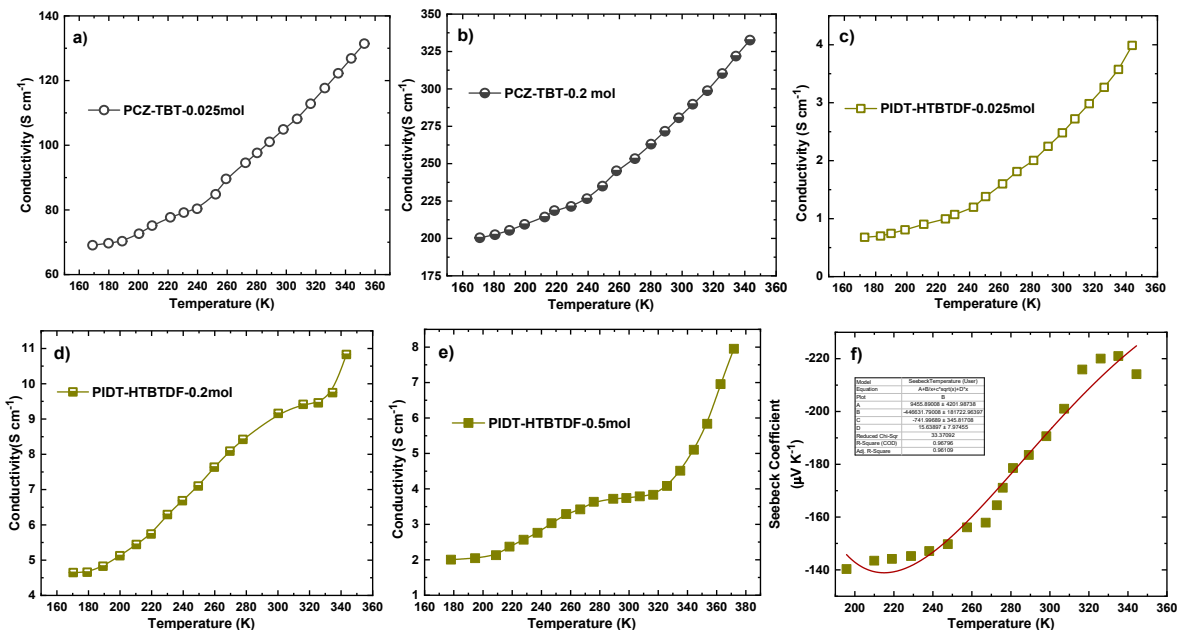


Figure S9. The temperature-dependence conductivities and Seebeck Coefficient of these samples. For PCZ-TBT doped with a) 0.025 M and b) 0.2 M FeCl_3 solutions, and PIDT-HTBTDF doped with c) 0.025 M d) 0.2 M and e) 0.5 M FeCl_3 solutions. f) temperature-dependence Seebeck coefficient of PIDT-HTBTDF doped with 0.5 M FeCl_3 solution.

Table S6. Effective temperature coefficients of A_1 , A_2 , A_3 and A_4 of the investigated polymer samples fitting according to the equation S1.

Polymers (FeCl_3 concentration)	A_1 [$\mu\text{V K}^{-1}$]	A_2 [$\mu\text{V K}^{-1}$]	A_3 [$\mu\text{V K}^{-1}$]	A_4 [$\mu\text{V K}^{-1}$]
PCZ-TBT (0.025 M)	-274.8	7580.5	28.7	-0.7
PCZ-TBT (0.2 M)	-40.2	-1384.3	6.3	-0.2
PID-HTBTDF (0.025 M)	-1172.6	19142.3	129.3	-3.3
PID-HTBTDF (0.2 M)	-24381.1	1044040	2021.6	-47.5

The temperature-dependence of Seebeck coefficient (S) measurements was performed to investigate the charge transport model of these polymer samples at different doping levels. According to the description of previously work, the temperature-dependence of S in doped polymer films can be fitted with the following equation (equation S1):²⁴

$$S(T) = A_1 + \frac{A_2}{T} + A_3\sqrt{T} + A_4T \quad (\text{equation S1})$$

wherein, A_1 , A_2 , A_3 , A_4 are fitting parameters, indicating the weightiness of different transport behavior, and the T is the absolute temperature in K. It has been reported that a linear response between the S and T can be observed in metallic type transport samples, while 3D variable range hopping transport displays a square root response to temperature, and 1D hopping type transport shows an inverse relationship between the S and temperature. In this respect, the contributions of different charge transfer models in the doped thin films can be identified according to the following key parameters.

X-Ray Diffraction measurements.

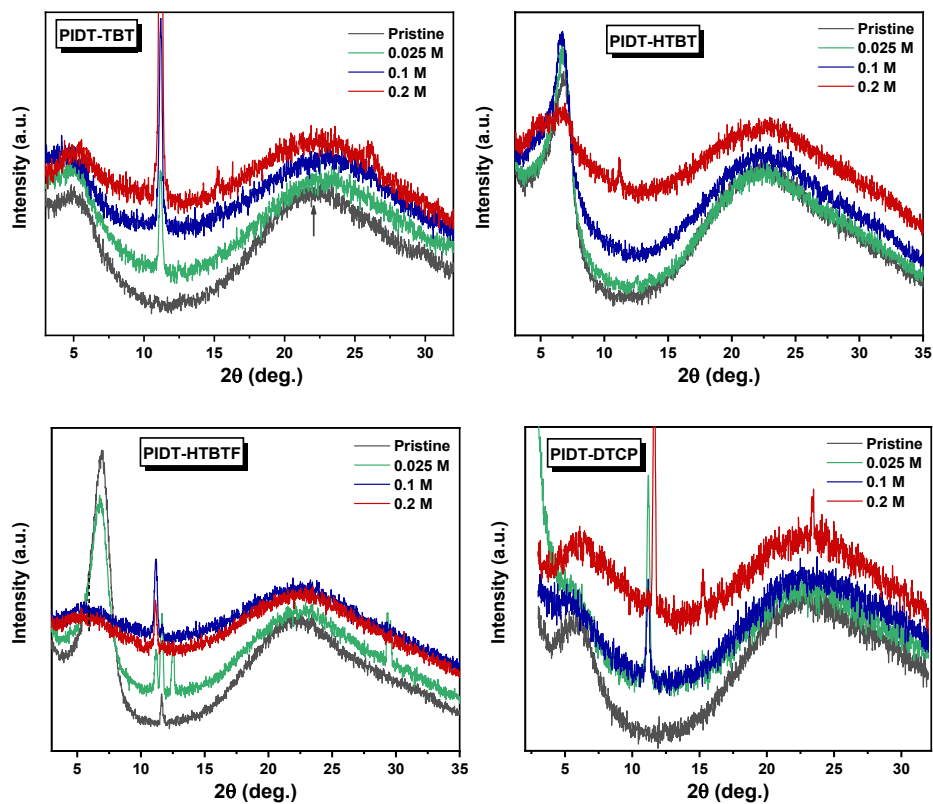


Figure S10. X-Ray diffraction spectra of these polymer samples doped with different FeCl_3 concentration. The intense diffraction peak at around $2\theta = 10^\circ$ is assigning to the remnant of FeCl_3 .²⁵

Theoretical calculations

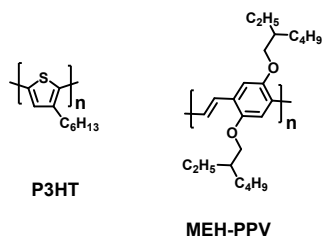


Figure S11. Chemical structure of P3HT and MEH-PPV.

To investigate the essential role of molecular parameters in contributing to their remarkable thermoelectric behaviors, the aforementioned six polymers together with P3HT and MEH-PPV (**Figure S9**) were calculated in parallel. According to the previously work, the S of P3HT and MEH-PPV can't be turned to negative regardless of the doping levels, while n-type charge transport can be observed on PCZ-TBT at high doping ratio.² Notably, PCZ-TBT in this work always display p-type charge transport properties with the FeCl₃ concentration range from 0.025 to 0.5 M, even though enhancing to 1.0 M, and doping time extending to 30 mins ($S = 18.2 \mu\text{V K}^{-1}$). These results indicated that a highly responsive S towards p-dopant concentrations is of vital important to develop efficient n-type thermoelectric materials whereby simple p-doping, which can be manipulated via molecular parameters optimization. On the other hand, although the electrical and thermal properties of the organic semiconductors sometimes were simulated following the first-principles calculations with precondition of periodic repeated array, for highly disordered amorphous polymer films, single molecular calculations relying on variable molecular parameters may provide more intuitive concept to understand the relationship between structure and property.⁵ The reality for organics is that the energetics for the entire system can usually be described by the energetics of the individual molecule or more broadly as a Gaussian density of states.²⁶ In this work, polymer models were treated as corresponding dimers with the alkyl chains were equivalent to methyl groups, while for P3HT and MEH-PPV, six repeat units were reserved to implement similar π -conjugation. The polymer models at ground states with closed-shell structures, are only considering spin “restricted” molecular orbitals. In radical cation forms (means an electron was removed from the neutral state after p-doping), both spin “restricted” and “unrestricted” molecular orbitals were used to describe the electronic structures of these open-shell molecules. In restricted case, an electron was removed from the primary HOMO after p-doping, and then split into two new orbitals, namely the lowest singly unoccupied

molecular orbital/the lowest singly occupied molecular orbital (SUMO/SOMO). In unrestricted case, considering the spin direction and electron occupancy, the frontier orbitals were marked with HOMO-alpha/HOMO-beta, LUMO-alpha/LUMO-beta, respectively.

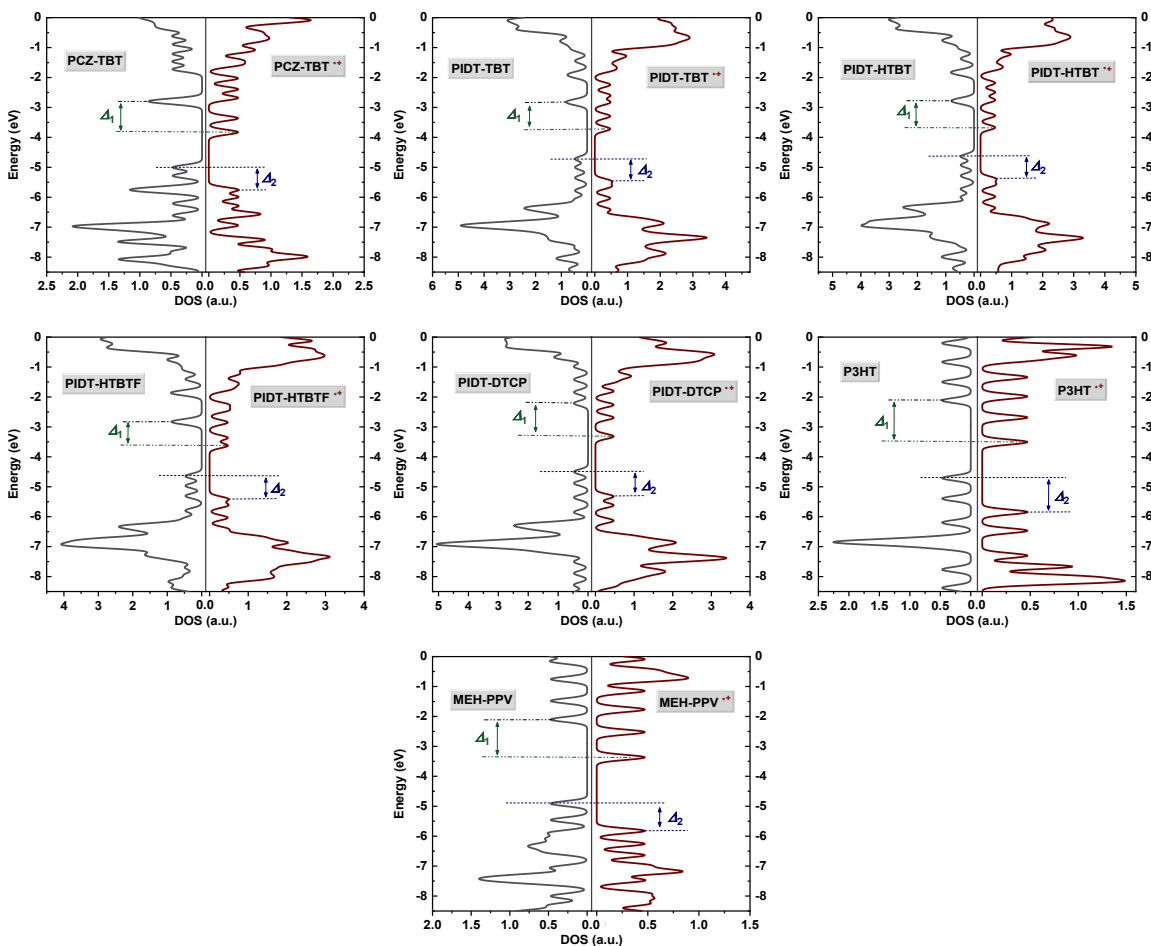


Figure S12. Comparison of the TDOS of these polymer models from the ground state (neutral, left) to corresponding radical cation state (right), with energy zero is aligned to vacuum and a Gaussian broadening of $\sigma = 0.2$ eV is applied for illustration purposes.

Table S7. The highest occupied molecular orbital (HOMO) and the lowest unoccupied molecular orbital (LUMO) distributions of these polymer models.

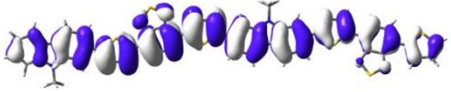
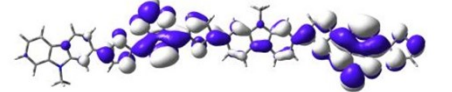
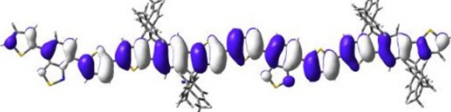
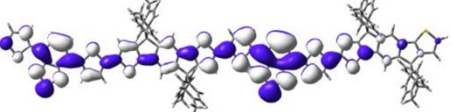
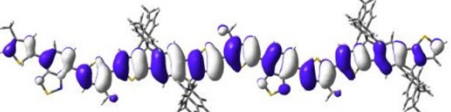
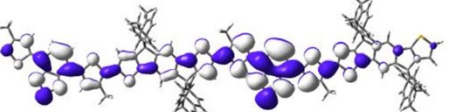
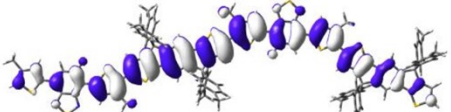
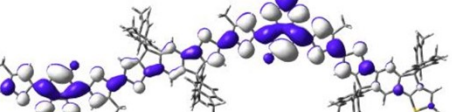
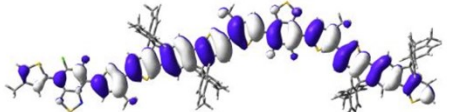
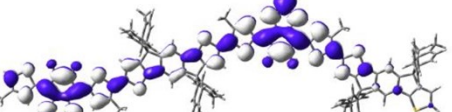
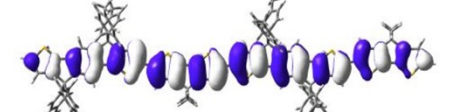
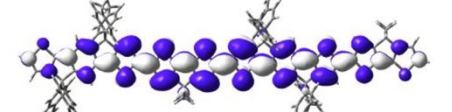
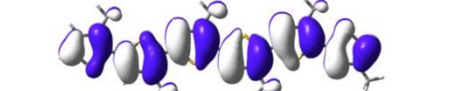
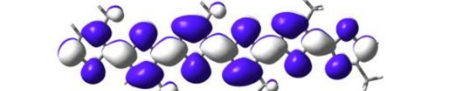

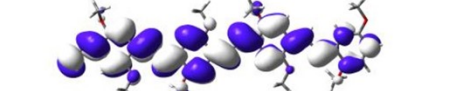
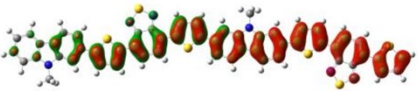
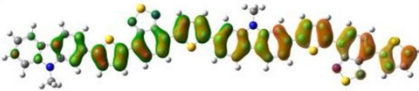
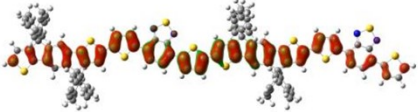
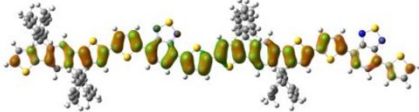
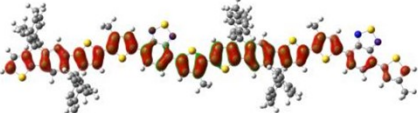
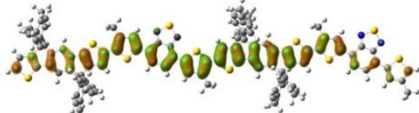
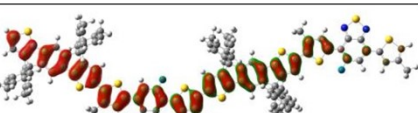
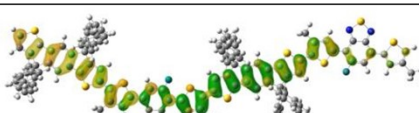
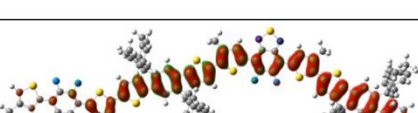
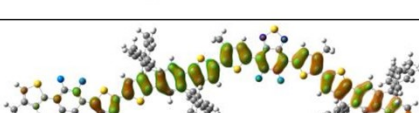

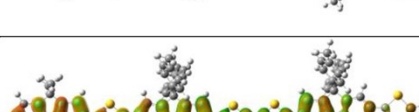
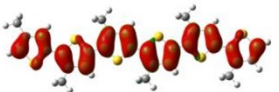
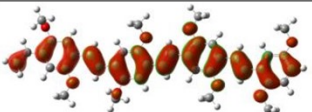
Polymer Models	HOMO	LUMO
PCZ-TBT		
PIDT-TBT		
PIDT-HTBT		
PIDT-HTBTF		
PIDT-HTBTDF		
PIDT-DTCP		
P3HT		
MEH-PPV		

Table S8. Orbital overlaps between the HOMO-alpha (red color) and LUMO-beta (green color), HOMO-beta (orange color) and LUMO-beta (green color) of these polymer models in radical cation forms.

Polymer Models	HOMO-alpha & LUMO-beta ^{a)}	HOMO-beta & LUMO-beta ^{a)}
PCZ-TBT		
PIDT-TBT		
PIDT-HTBT		
PIDT-HTBTF		
PIDT-HTBTDF		
PIDT-DTCP		
P3HT		$E_g = 1.29 \text{ eV}^{\text{b}}$
MEH-PPV		$E_g = 1.1 \text{ eV}^{\text{b}}$

^{a)}isovalue 0.02, ^{b)}energy gaps is too large.

Table S9. Surface electrostatic potential distribution of these polymer models from neutral to radical cation form.

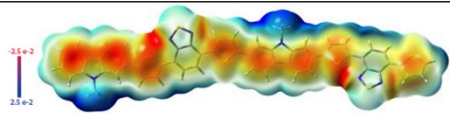
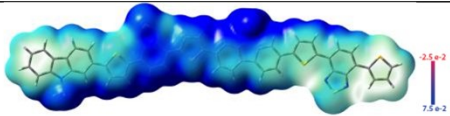
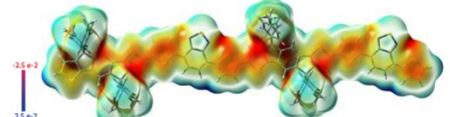
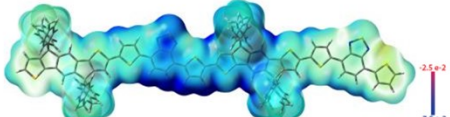
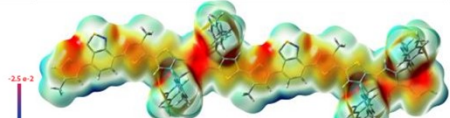
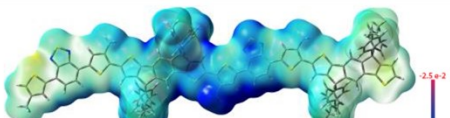
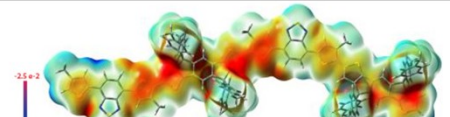
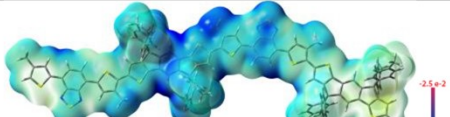
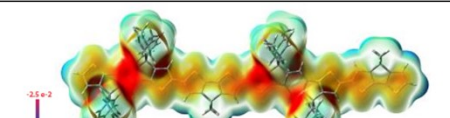
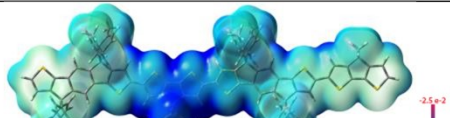
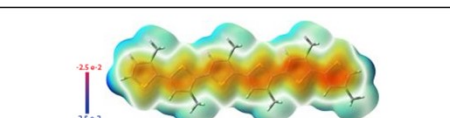
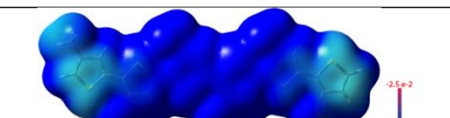
Polymer Models	Neutral state	Radical cation state
PCZ-TBT		
PIDT-TBT		
PIDT-HTBT		
PIDT-HTBTF		
PIDT-DTCP		
P3HT		

Table S10. Calculated energy levels and ω values of these polymer models at different states.

Polymers	LUMO/HOMO [eV] ^{a)}	LUMO [eV] ^{b)}	HOMO [eV] ^{b)}	SUMO [eV] ^{c)}	SOMO [eV] ^{c)}	ω ^{d)}
PCZ-TBT	-2.83/-5.00	-3.83/ -5.11	-5.75/ -5.69	-5.88	-7.71	0.1264
PIDT-TBT	-2.87/-4.72	-3.72/ -4.83	-5.45/ -5.43	-5.39	-7.50	0.1398
PIDT-HTBT	-2.83/-4.64	-3.67/ -4.75	-5.38/ -5.37	-5.30	-7.10	0.1043
PIDT-HTBTF	-2.87/-4.63	-3.62/ -4.78	-5.41/ -5.40	-5.32	-6.99	0.0972
PIDT-HTBTDF	-2.90/-4.73	-3.67/ -4.84	-5.46/ -5.41	-5.40	-7.09	0.0963
PIDT-DTCP	-2.21/-4.50	-3.32/ -4.61	-5.32/ -5.36	-5.17	-7.17	0.1045
P3HT	-2.12/-4.70	-3.50/ -4.87	-5.84/ -6.16	-5.65	-8.69	0.1574
MEH-PPV	-2.10/-4.91	-3.37/ -4.92	-5.82/ -6.02	-5.55	-8.10	0.1271

^{a)}Calculated HOMO and LUMO levels of these polymers at ground state with optimal geometrical configuration at the b3lyp/def2svp level, ^{b)}calculated HOMO and LUMO energy levels of these polymers at corresponding radical cation form, with the sequence of alpha/beta orbitals at the b3lyp/def2svp level, ^{c)}the highest singly occupied molecular orbital (SOMO) and the lowest singly unoccupied molecular orbital (SUMO) were splitted from the neutral HOMO orbital after p-doping procedure, and the values were calculated according to the optimized LC- ω pbe/def2svp level of theory, ^{d)}the optimized ω values for different polymer models.

Table S11. Overlaps of these frontier molecular orbitals at radical cation state, following the sequence of centroid distance between the two orbitals (Angstrom), and overlap integral of norm of the two orbitals.

Polymers	HOMO- α & LUMO- α	HOMO- β & LUMO- β	HOMO- α & HOMO- β	LUMO- α & LUMO- β	HOMO- α & LUMO- β	LUMO- α & HOMO- β
PCZ-TBT ⁺	12.26, 0.479	7.17, 0.798	1.06, 0.925	4.08, 0.675	8.22, 0.882	11.21, 0.505
PIDT-TBT ⁺	3.46, 0.614	0.244, 0.795	0.230, 0.907	3.85, 0.671	0.416, 0.966	3.68, 0.543
PIDT-HTBT ⁺	2.79, 0.620	1.59, 0.745	0.126, 0.904	4.44, 0.664	1.69, 0.963	2.88, 0.553
PIDT-HTBTF ⁺	2.88, 0.635	7.17, 0.831	0.845, 0.914	6.37, 0.641	7.68, 0.892	3.19, 0.578
PIDT-HTBTDF ⁺	2.46, 0.617	4.14, 0.816	0.705, 0.918	4.63, 0.644	4.49, 0.951	3.00, 0.566
PIDT-DTCP ⁺	5.54, 0.698	5.43, 0.787	1.45, 0.903	1.55, 0.787	3.98, 0.951	6.99, 0.633
P3HT ⁺	0.758, 0.781	0.750, 0.803	0.494, 0.848	1.01, 0.799	0.255, 0.991	0.263, 0.737
MEH-PPV ⁺	1.04, 0.789	2.00, 0.757	0.172, 0.860	0.899, 0.816	1.94, 0.968	1.12, 0.687

In doped polymer semiconductors, the energy gaps between neighboring occupied and unoccupied orbitals are gradually narrowed with the increase of doping levels, and therefore, thermal-induced intrinsic excitation play an important role to enhance their conductivities and S . In this respect, overlaps between occupied orbitals and neighboring unoccupied orbitals enable a potential channel to realize thermal-inspired electron transfer. On the other hand, the electrostatic interactions are largely depended on the centroid distance between the two orbitals (**Table S9**),

which determine the moving of electron and hole between neighboring conjugated polymer chains. When the neighboring energy gaps are too wide, consideration of orbital overlaps is insignificant.

References

1. F. Zhong, X. Yin, Z. Chen, C. Gao, L. Wang, *ACS Appl. Mater. Interfaces*, 2020, **12**, 26276-26285.
2. Z. Liang, H. H. Choi, X. Luo, T. Liu, A. Abtahi, U. S. Ramasamy, J. A. Hitron, K. N. Baustert, J. L. Hempel, A. M. Boehm, A. Ansary, D. R. Strachan, J. Mei, C. Risko, V. Podzorov, K. R. Graham, *Nat. Mater.*, 2021, **20**, 518-524.
3. T. Lu, F. Chen, *J. Comput. Chem.*, 2012, **33**, 580-592.
4. D. X. Xie, T. C. Liu, J. Xiao, J. K. Fang, C. J. Pan, G. Shao, *Molecules*, 2021, **26**, 963.
5. B. Russ, A. Glauddell, J. J. Urban, M. L. Chabiny, R. A. Segalman, *Nat. Rev. Mater.*, 2016, **1**, 16050.
6. N. B. Re'da Badrou Aïch, Ange'lique Bouchard, and Mario Leclerc, *Chem. Mater.*, 2009, **21**, 751-757.
7. J. Liu, Y. Shi, J. Dong, M. I. Nugraha, X. Qiu, M. Su, R. C. Chiechi, D. Baran, G. Portale, X. Guo, L. J. A. Koster, *ACS Energy Lett.*, 2019, **4**, 1556-1564.
8. Y. Lu, Z.-D. Yu, R.-Z. Zhang, Z.-F. Yao, H.-Y. You, L. Jiang, H.-I. Un, B.-W. Dong, M. Xiong, J.-Y. Wang, J. Pei, *Angew. Chem. Int. Ed.*, 2019, **58**, 11390-11394.
9. X. Yan, M. Xiong, J. T. Li, S. Zhang, Z. Ahmad, Y. Lu, Z. Y. Wang, Z. F. Yao, J. Y. Wang, X. Gu, T. Lei, *J. Am. Chem. Soc.*, 2019, **141**, 20215-20221.
10. M. Alsufyani, R. K. Hallani, S. Wang, M. Xiao, X. Ji, B. D. Paulsen, K. Xu, H. Bristow, H. Chen, X. Chen, H. Sirringhaus, J. Rivnay, S. Fabiano, I. McCulloch, *J. Mater. Chem. C*, 2020, **8**, 15150-15157.
11. M.-K. Jeong, E. H. Suh, K. Lee, J. Jang, I. H. Jung, *Org. Electron.*, 2020, **86**, 105921.
12. J. Liu, G. Ye, H. G. O. Potgieser, M. Koopmans, S. Sami, M. I. Nugraha, D. R. Villalva, H. Sun, J. Dong, X. Yang, X. Qiu, C. Yao, G. Portale, S. Fabiano, T. D. Anthopoulos, D. Baran, R. W. A. Havenith, R. C. Chiechi, L. J. A. Koster, *Adv. Mater.*, 2020, **33**, 2006694.
13. Y. Wang, K. Takimiya, *Adv. Mater.*, 2020, **32**, 2002060.
14. H. Chen, M. Moser, S. Wang, C. Jellett, K. Thorley, G. T. Harrison, X. Jiao, M. Xiao, B. Purushothaman, M. Alsufyani, H. Bristow, S. De Wolf, N. Gasparini, A. Wadsworth, C. R. McNeill, H. Sirringhaus, S. Fabiano, I. McCulloch, *J. Am. Chem. Soc.*, 2021, **143**, 260-268.
15. C. Dong, S. Deng, B. Meng, J. Liu, L. Wang, *Angew. Chem. Int. Ed. Engl.*, 2021, **60**, 16184-16190.
16. K. Feng, H. Guo, J. Wang, Y. Shi, Z. Wu, M. Su, X. Zhang, J. H. Son, H. Y. Woo, X. Guo, *J. Am. Chem. Soc.*, 2021, **143**, 1539-1552.
17. J. Han, C. Ganley, Q. Hu, X. Zhao, P. Clancy, T. P. Russell, H. E. Katz, *Adv. Funct. Mater.*, 2021, **31**, 2010567.
18. C.-Y. Yang, W.-L. Jin, J. Wang, Y.-F. Ding, S. Nong, K. Shi, Y. Lu, Y.-Z. Dai, F.-D. Zhuang, T. Lei, C.-A. Di, D. Zhu, J.-Y. Wang, J. Pei, *Adv. Mater.*, 2018, **30**, 1802850.
19. S. Wang, H. Sun, T. Erdmann, G. Wang, D. Fazzi, U. Lappan, Y. Puttisong, Z. Chen, M. Berggren, X. Crispin, A. Kiriy, B. Voit, T. J. Marks, S. Fabiano, A. Facchetti, *Adv. Mater.*, 2018, **30**, 1801898.
20. Y. Lu, Z. D. Yu, H. I. Un, Z. F. Yao, H. Y. You, W. Jin, L. Li, Z. Y. Wang, B. W. Dong, S. Barlow, E. Longhi, C. A. Di, D. Zhu, J. Y. Wang, C. Silva, S. R. Marder, J. Pei, *Adv. Mater.*, 2021, **33**, 2005946.
21. H. Zeng, M. Mohammed, V. Untilova, O. Boyron, N. Berton, P. Limelette, B. Schmaltz, M. Brinkmann, *Adv. Electron. Mater.*, 2021, **7**, 2000880.
22. J. Wang, Y. Wang, Q. Li, Z. Li, K. Li, H. Wang, *CCS Chem.*, 2021, **3**, 2482-2493.
23. J. Wang, Y. Wang, K. Li, X. Dai, L. Zhang, H. Wang, *Adv. Mater.*, 2022, **34**, 2106624.

24. J. Joo, S. M. Long, J. P. Pouget, E. J. Oh, A. G. MacDiarmid, A. J. Epstein, *Phys. Rev. B*, 1998, **57**, 9567-9580.
25. E. M. Abdelrazek, *Physica B: Condensed Matter*, 2007, **400**, 26-32.
26. N. Lu, L. Li, M. Liu, *Phys. Chem. Chem. Phys.*, 2016, **18**, 19503-19525.